

A machine-learning pipeline for real-time detection of gravitational waves from compact binary coalescences

Ethan Marx

emarx@mit.edu

Massachusetts Institute of Technology

William Benoit

University of Minnesota

Alec Gunny

Massachusetts Institute of Technology

Rafia Omer

University of Minnesota

Deep Chatterjee

Massachusetts Institute of Technology

Ricco Venterea

Cornell University

Lauren Wills

University of Minnesota

Muhammed Saleem

University of Minnesota

Eric Moreno

Massachusetts Institute of Technology

Ryan Raikman

Carnegie Mellon University

Ekaterina Govorkova

Massachusetts Institute of Technology

Dylan Rankin

University of Pennsylvania

Michael Coughlin

University of Minnesota <https://orcid.org/0000-0002-8262-2924>

Philip Harris

Massachusetts Institute of Technology

Erik Katsavounidis

Article

Keywords:

Posted Date: May 15th, 2024

DOI: <https://doi.org/10.21203/rs.3.rs-4271631/v1>

License:  This work is licensed under a Creative Commons Attribution 4.0 International License.

[Read Full License](#)

Additional Declarations: There is **NO** Competing Interest.

1 A machine-learning pipeline for real-time detection of 2 gravitational waves from compact binary coalescences

³ Ethan Marx^{1,2,*}, William Benoit^{3,*}, Alec Gunny^{1,2,*}, Rafia Omer³, Deep Chatterjee^{1,2}, Ricco C. Venterea^{3,5},
⁴ Lauren Wills³, Muhammed Saleem³, Eric Moreno^{1,2}, Ryan Raikman^{1,6}, Ekaterina Govorkova^{1,2},
⁵ Dylan Rankin⁴, Michael W. Coughlin³, Philip Harris¹, Erik Katsavounidis^{1,2}

⁶ ¹*Department of Physics, MIT, Cambridge, MA 02139, USA*

⁷ ²*LIGO Laboratory, 185 Albany St, MIT, Cambridge, MA 02139, USA*

⁸ ³*School of Physics and Astronomy, University of Minnesota, Minneapolis, Minnesota 55455, USA*

⁹ ⁴*Department of Physics and Astronomy, University of Pennsylvania, Philadelphia, PA, 19104,
10 USA*

¹¹ ⁵*Department of Astronomy, Cornell University, Ithaca, NY, 14853, USA*

¹² ⁶*Department of Physics, Carnegie Mellon University, Pittsburgh, PA, 15213*

¹³ **The promise of multi-messenger astronomy relies on the rapid detection of gravitational
14 waves at very low latencies ($\mathcal{O}(1\text{ s})$) in order to maximize the amount of time available for
15 follow-up observations. In recent years, neural-networks have demonstrated robust non-linear
16 modeling capabilities and millisecond-scale inference at a comparatively small computational
17 footprint, making them an attractive family of algorithms in this context. However, integration
18 of these algorithms into the gravitational-wave astrophysics research ecosystem has proven
19 non-trivial. Here, we present the first fully machine learning-based pipeline for the detection
20 of gravitational waves from compact binary coalescences (CBCs) running in low-latency. We
21 demonstrate this pipeline to have a fraction of the latency of traditional matched filtering
22 search pipelines while achieving state-of-the-art sensitivity to higher-mass stellar binary black
23 holes.**

²⁴ Gravitational-wave astronomy has developed rapidly since the first direct detection of gravitational
25 waves from a binary black hole merger in 2015¹, with new detections now a common occurrence².
26 With the fourth observing run (O4) of the International Gravitational-wave Network (IGWN),
27 consisting of LIGO³, Virgo⁴, and KAGRA⁵ already underway, and with future ground and space
28 based detectors planned for various points in the next decade^{6–8}, ever more frequent discoveries of
29 gravitational waves will enable follow-up observation of events across other cosmic messengers

*These authors contributed equally to this work

30 such as electromagnetic radiation and astrophysical neutrinos^{9–14}. The insights we gain in this era
31 of multi-messenger astrophysics will directly correlate with the volume and diversity of data we
32 are able to collect.

33 While machine learning (ML) is ubiquitous in some areas of physics¹⁵, it has only recently
34 approached a stage of maturity in the gravitational-wave community. To date, there have been a
35 number of machine learning models proposed for the detection of compact binary coalescences
36 (CBCs); e.g.,^{16–20}; but there are none currently running in O4²¹ (though, ML-based unmodeled
37 gravitational-wave searches have seen production usage²²). This is both a product of well-known
38 infrastructure hurdles separating the development and deployment of machine learning models²³,
39 as well as a lack of standardized, astrophysically meaningful probes of the sensitivity of these
40 models in the face of non-stationary and transient background noise.

41 The most well-modeled and frequently observed gravitational-wave events to date are the
42 mergers of binary black hole (BBH) systems^{2,24,25}. Their comparatively high number of confirmed
43 detections has given us reasonable models of their population statistics, allowing for astrophysically
44 meaningful measures of search sensitivity. BBH mergers also benefit from a highly localized-in-time
45 signal-to-noise ratio (SNR) profile relative to binary neutron star (BNS) mergers, which are in the
46 sensitive band of the detectors much longer. Studying the ability of neural-networks to detect BBH
47 mergers, and in particular what real time use in the IGWN detectors looks like in this context,
48 represents an important first step towards developing a more thorough understanding of how, and
49 whether, these algorithms can be applied to more challenging signals such as BNSs, and what tools
50 and infrastructure would be required to do so.

51 Here, we present `Aframe`, a flexible pipeline for detection of BBH mergers using deep
52 learning. The implementation presented here uses a 1D convolutional neural-network. Convolutional
53 neural-networks have previously been shown to have potential for gravitational wave detection²⁶,
54 and we use this architecture, along with aggressive data augmentation techniques, to achieve a
55 sensitivity competitive with matched filtering CBC search pipelines while requiring a significantly
56 lower latency. More broadly, `Aframe` encompasses a suite of tools for quickly implementing,
57 testing, and deploying new ideas at scale in order to more confidently realize the potential of
58 machine learning in service to gravitational wave astronomy.

59 Our neural-network architecture modifies a standard ResNet54²⁷, which maps fixed length
60 time-series of gravitational wave strain from two interferometers (here, the Hanford and Livingston
61 LIGO interferometers) to a scalar detection statistic indicating whether a signal is present in
62 the input. Critically, we replace 2D with 1D convolutions to accommodate time-series input.
63 In addition, we replace standard Batch Normalization layers (BN)²⁸, with Group Normalization
64 (GN) layers²⁹. While BN layers fit parameters to statistics calculated along the batch dimension,
65 GN layers are fit to statistics calculated from groups of channels. This choice was motivated by
66 differences in the statistical properties of batches during training and inference. During training,
67 there are significantly more signals in each batch than during inference, where most of the batch
68 consists of noise. Thus, during training, BN layers will learn spurious statistical properties that are
69 not present at inference time. GN layers mitigate this problem by learning statistical properties of
70 individual channels. We found that using GN layers improves the agreement between validation
71 and test time metrics, as well as overall testing performance. Good agreement between validation
72 and test metrics is essential for ensuring the best neural-network is being selected for deployment.
73 The neural-network is trained by minimizing a binary cross entropy loss function with an Adam³⁰
74 optimizer. We use a one cycle learning rate scheduler with cosine annealing³¹.

75 Analyzing data with `Aframe` involves loading and preprocessing timeseries data, breaking
76 it up into short time segments, then passing these segments through the neural-network. The
77 throughput associated with each of these steps can vary drastically, as can the hardware and
78 software necessary to accelerate them. In order to optimize the total throughput of this system,
79 we adopt an inference-as-a-service (IaaS) computing model in which neural-network inference is
80 handled by a dedicated service, to which client applications can send inference requests remotely.
81 Each step in our pipeline is then implemented and scaled independently to most efficiently leverage
82 a fixed pool of heterogeneous computing resources. This model has been shown to be effective in
83 optimizing ML inference in GW astronomy³², provided that “snapshotting”³³ is used to cache
84 overlapping input data on the server side to avoid redundant data transfer. We adopt this paradigm
85 using an off-the-shelf IaaS implementation, Triton Inference Server³⁴, and use the ML inference
86 framework TensorRT to accelerate the neural-network inference step. The ability to scale and
87 distribute a workload is an important part of any search pipeline, and the authors are aware of
88 only one other ML-based CBC detection algorithm that has focused on scalability to arbitrary
89 resources³⁵. In the sections below, we compare both our sensitivity and our throughput to this
90 work.

91 Inference is performed at a rate of 4 Hz (not to be confused with the neural-network throughput,
 92 see the discussion of computational requirements below). In other words, we pass windows of
 93 data to our neural-network for inference such that each window is shifted by 0.25 s. This inference
 94 sampling rate reduces the overall compute load without sacrificing search sensitivity (see Sec. 4
 95 of Methods). These neural-network predictions are then integrated over time using a 1 s top hat
 96 filter (see Fig. 1). Because the neural-network is trained to encode time translation invariance (see
 97 Sec. 2 of Methods), we expect to see a consistently high neural-network responses when analyzing
 98 astrophysical signals. Thus, integration provides a mechanism to promote consistently high outputs
 99 while rejecting short transients that may correspond to non-astrophysical sources. Finally, the
 100 integrated time-series of neural-network predictions is clustered to avoid yielding multiple triggers
 101 for the same event. The maximum integrated value over an 8 s window is taken as the detection
 102 statistic corresponding to a candidate event.

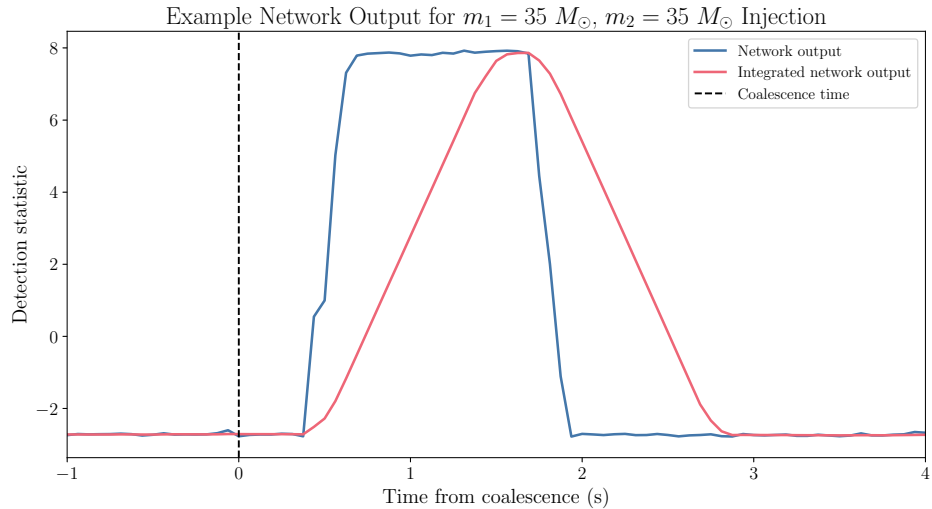


Figure 1: Example neural-network prediction and integrated neural-network prediction for a $m_1 = 35 M_\odot, m_2 = 35 M_\odot$ signal injection. The coalescence time is plotted as the vertical dashed black line. The brief gap between coalescence time and beginning of neural-network activation is due to the fact that we do not inject the coalescence time in the first or last 0.25 s of the window during training.

103 To demonstrate `Aframe`’s readiness for real-time deployment, we compare its sensitivity
 104 to search pipelines used in production by IGWN. For our pipeline, estimating sensitive volume
 105 requires analyzing simulated GW events “injected” into strain data, and analyzing background
 106 livetime produced by “timeslides.” Performing timeslides is a standard way of empirically estimating

107 the background (i.e. the distribution of noise events) for a search pipeline which analyzes a network
108 of detectors. In brief, the strain from one detector is shifted in time by an amount greater than
109 the gravitational wave travel time between the detectors (~ 10 ms for the two LIGO detectors).
110 Therefore, any reported triggers could not have been caused by an astrophysical event. In this
111 analysis, the Hanford strain data is held fixed and the Livingston data is shifted in 1 s increments
112 until the required background livetime is accumulated. Then, a false alarm rate (FAR) can be
113 assigned to injected events by dividing the number of background events with detection statistic
114 greater than the event of interest, with livetime analyzed. All GW detections reported in the third
115 Gravitational-Wave Transient Catalog (GWTC-3)² were excised from the background.

116 **Comparison with existing searches.** A useful metric to measure the sensitivity of search
117 algorithms is the *sensitive volume*. Sensitive volume measures the volume over which some
118 astrophysical population of sources distributed uniformly in co-moving volume is detectable at
119 a given false alarm rate (FAR). Sensitive volume was used to measure the sensitivity of search
120 pipelines in GWTC-3. This provides an astrophysically meaningful benchmark to compare the
121 performance of `Aframe` to the performance of traditional searches. More details on the sensitive
122 volume calculation can be found in Sec. 3 of Methods. Fig. 2 compares `Aframe`'s sensitive
123 volume as a function of FAR with the sensitivity of the MBTA³⁷, PyCBC³⁸, GstLAL^{39,40} and
124 cWB⁴¹ searches as reported in GWTC-3². We note that the template banks used by MBTA,
125 GstLAL, and PyCBC-Broad in the GWTC-3 analysis contain waveforms outside of the $5-100$ M $_{\odot}$
126 range searched by `Aframe`. In principle, these searches could increase their sensitivities in the
127 $5-100$ M $_{\odot}$ range by removing these templates. This is evident when comparing the performance
128 of PyCBC-BBH and PyCBC-Broad in Fig. 2. For the future, we encourage production level LVK
129 CBC pipelines to publish BBH-specific sensitivities against which developing ML pipelines can
130 benchmark.

131 In the $35-35$ M $_{\odot}$ mass distribution, `Aframe` has a larger sensitive volume than the GWTC-3
132 configurations of all searches, and is comparable in the $35-20$ M $_{\odot}$ mass bin, for the FARs considered
133 in this analysis. As source masses decrease further, so does `Aframe`'s performance relative to
134 existing pipelines. This is in part due to our neural-network architectures inability to model the
135 lower frequency features of these low mass signals. While the architecture implements global
136 pooling layers, the convolution layers use a kernel length of 3 samples. Improvements to neural-network
137 architecture design, such as utilizing dilated convolutions that can better model these lower frequency

138 features will help to improve performance at these mass ranges.

139 Previous studies of ML-based gravitational wave detection algorithms tend not to use sensitive
140 volume as a metric, preferring instead to use traditional ML metrics such as receiver operating
141 characteristic (ROC) curves (an exception is⁴², which uses a non-astrophysical prior and a Euclidean
142 volume distribution). This makes direct comparison difficult, as these metrics depend on the
143 parameter distributions of tested events. For the sake of completeness, in Fig. 3 we present our
144 own ROC curve and find that, compared to previous works^{35,43}, we achieve nearly three orders
145 of magnitude of improvement in true positive rate at a false positive rate of $\sim 10^{-6}$ for an SNR
146 threshold of 6.23, where most astrophysical events are. However, we encourage future studies to
147 use sensitive volume to astrophysically motivated distributions as the measure of performance.

148 **Detecting Astrophysical Candidates in GWTC-3.** The testing period we use contains 9
149 astrophysical candidate events reported as significant detections in GWTC-3. While we evaluated
150 our algorithm’s performance using “timeslides” of this data (see Sec. 4 of Methods), we also
151 analyzed the unshifted (or “zero-lag”) data to determine if our algorithm detects these known
152 candidates. The results of this analysis are shown in Table 1. We detect all 9 candidates, with 8
153 of the 9 candidates detected at a false alarm rate of less than 1 per year, the minimum possible
154 value for this analysis. For the final event, our reported false alarm rate, 14 per year, is of a similar
155 magnitude to the false alarm rate reported by the GWTC-3 pipelines at 2.8 per year. Additionally,
156 during this period, we do not report any non-catalog candidates with a false alarm rate less than 5
157 per month.

158 **Latency and Computational Requirements.** Training the neural-network with a single
159 NVIDIA 16 GB Tesla V100 GPU takes approximately 43 hours, and once trained, the neural-network
160 can continue to be used for months without retraining; see the discussion of algorithm longevity
161 in Sec. 2 for details. For inference, we utilize a Triton inference server³⁴ that is hosted on a
162 NVIDIA DGX server containing eight 16 GB Tesla V100 GPUs (See Sec. 4 for details on inference
163 configuration). Altogether, analyzing the one year of background data and one year of injections
164 used in this analysis to create Fig. 2 takes approximately 4 hours, corresponding to a throughput
165 of about 500 seconds of data from a two detector network analyzed per second per GPU. This
166 corresponds to an order of magnitude improvement in throughput compared with previous work
167 by Huerta et al³⁵ and a factor of ~ 2.5 compared with Chatruvedi et al⁴³. This improvement is

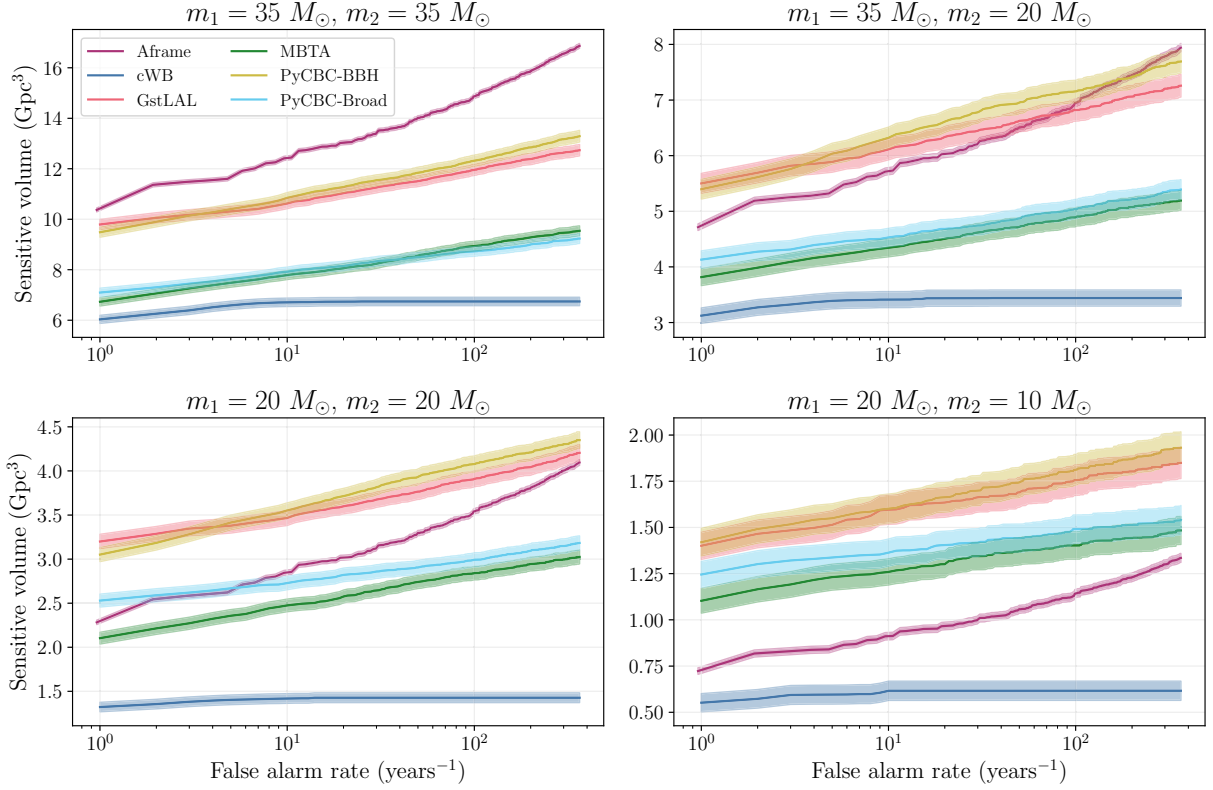


Figure 2: Sensitive volume vs FAR for four different mass distributions. Masses are specified in the source frame. Each mass is drawn from a log-normal distribution with a mean of the value given above each plot and a width of 0.1. Aframe demonstrates state-of-the-art sensitivity at higher masses, but loses performance relative to traditional search pipelines at lower masses. The sensitive volume of the other pipelines was calculated using data from a GWTC-3 data release⁴⁴.

¹⁶⁸ due to the use of a more efficient neural-network architecture, as well as the IaaS model described
¹⁶⁹ above.

¹⁷⁰ With trained neural-network weights in hand, the requirements for online deployment are
¹⁷¹ much smaller. A single NVIDIA 24 GB A30 GPU is sufficient for real-time inference at an
¹⁷² inference sampling rate of 2048 Hz, which provides sufficient resolution for coalescence time
¹⁷³ estimation. The total memory required to hold both the neural-network and data is 4.6 GB. The
¹⁷⁴ computational latency of the neural-network is less than 10 milliseconds. In practice, the latency
¹⁷⁵ of our algorithm is dominated by pre- and post-processing steps that bring the total latency to

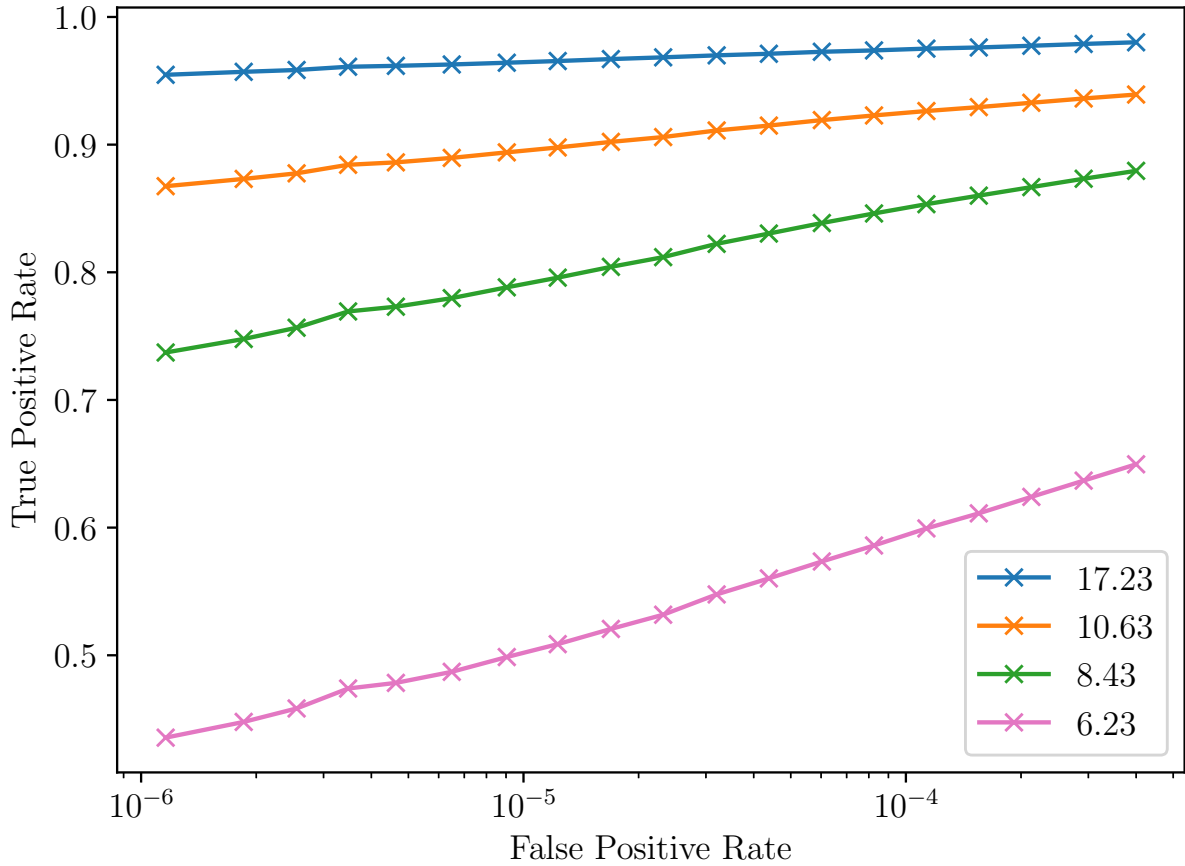


Figure 3: ROC curves for waveforms in different SNR bins in our testing dataset, described in Sec. 1. Each bin contains waveforms with SNRs at or above the given value.

approximately 3.1 s. For a detailed accounting of sources of latency within `Aframe`, see Sec. 4. In production, additional latency is incurred uploading events to the GRAvitational-wave Candidate Event DataBase (GraceDB)⁴⁶. This latency is not included in this 3.1 s estimate. In addition, a recent study⁴⁶ used a real-time mock data challenge replay of O3 data to benchmark pipeline latencies, including GraceDB processing. Analyzing this data stream, we find a median (90%) event reporting latency of 3.9 s (4.3 s), in good agreement with our latency budget. Matched filtering pipelines report a median (90%) latency of 12.3 s (41.4 s).

Discussion. We have implemented a machine-learning based CBC search pipeline that is

⁴⁶<https://gracedb.ligo.org/>

184 capable of low-latency use in a production setting. Through robust data augmentation techniques
185 and extensive work in developing software infrastructure (Sec. 5), our algorithm achieves a sensitivity
186 that is competitive with established search pipelines for higher mass BBHs. Work remains to
187 improve the algorithm’s performance on lower mass BBH systems. We leave these investigations
188 to future work.

189 There are a number of extensions we plan to investigate in future work. Our algorithm is
190 currently limited to the use of data from exactly two interferometers, and this limits our flexibility.
191 In this work we trained our neural-network on data from the two LIGO interferometers, but we
192 could benefit from the ability to include Virgo and KAGRA data. This could take the form of a
193 four-detector model, or could be a suite of pairwise models that work in unison. Additionally,
194 allowing for single-detector analysis would be beneficial for instances where only one detector is
195 online. Further, low-latency alerts are less important for BBHs than binary neutron star (BNS)
196 and neutron star-black hole (NSBH) mergers, where electromagnetic counterparts are more likely.
197 The detection of these mergers with neural-networks is more challenging due to the greater length
198 of time these signals spend in the sensitive band of the detector. Still, preliminary explorations
199 indicate that our framework can adapt to address this problem.

Event	$m_1(M_\odot)$	$m_2(M_\odot)$	Aframe	cWB	GstLAL	MBTA	PyCBC-BBH	PyCBC-Broad
GW190512_180714	$23.2^{+5.6}_{-5.6}$	$12.5^{+3.5}_{-2.6}$	< 0.97	0.88	$< 1.0 \times 10^{-5}$	0.038	$< 1.1 \times 10^{-4}$	1.1×10^{-4}
GW190513_205428	$36.0^{+10.6}_{-9.7}$	$18.3^{+7.4}_{-4.7}$	< 0.97	–	1.3×10^{-5}	0.11	0.044	19
GW190514_065416	$40.9^{+17.3}_{-9.3}$	$28.4^{+10.0}_{-10.1}$	14	–	450	–	2.8	–
GW190517_055101	$39.2^{+13.9}_{-9.2}$	$24.0^{+7.4}_{-7.9}$	< 0.97	0.0065	0.0045	0.11	3.5×10^{-4}	0.0095
GW190519_153544	$65.1^{+10.8}_{-11.0}$	$40.8^{+11.5}_{-12.7}$	< 0.97	3.1×10^{-4}	$< 1.0 \times 10^{-5}$	7.0×10^{-5}	$< 1.1 \times 10^{-4}$	$< 1.0 \times 10^{-4}$
GW190521	$98.4^{+33.6}_{-21.7}$	$57.2^{+27.1}_{-30.1}$	< 0.97	2.0×10^{-4}	0.20	0.042	0.0013	0.44
GW190521_074359	$43.4^{+5.8}_{-5.5}$	$33.4^{+5.2}_{-6.8}$	< 0.97	1.0×10^{-4}	$< 1.0 \times 10^{-5}$	1.0×10^{-5}	$< 2.3 \times 10^{-5}$	$< 1.8 \times 10^{-5}$
GW190527_092055	$35.6^{+18.7}_{-8.0}$	$22.2^{+9.0}_{-8.7}$	< 0.97	–	0.23	–	19	–
GW190602_175927	$71.8^{+18.1}_{-14.6}$	$44.8^{+15.5}_{-19.6}$	< 0.97	0.015	$< 1.0 \times 10^{-5}$	3.0×10^{-4}	0.013	0.29

Table 1: Masses in units of M_\odot , and false alarm rates in units of inverse years from Aframe, cWB, GstLAL, MBTA, and PyCBC-BBH for the known events in our testing set. Masses come from Table VIII of GWTC-2.1²⁵, and FARs from Table XV of GWTC-3². As our analysis examined only one year of background, our minimum FAR is one per year.

201 1. Abbott et al. Observation of gravitational waves from a binary black hole merger. *Phys. Rev.*
200 *Lett.* **116**, 061102 (2016).

203 2. Abbott, R. *et al.* Gwtc-3: Compact binary coalescences observed by ligo and virgo during the
204 second part of the third observing run. *Physical Review X* **13** (2023). URL <http://dx.doi.org/10.1103/PhysRevX.13.041039>.

206 3. The LIGO Scientific Collaboration *et al.* Advanced ligo. *Classical and Quantum Gravity*
207 **32**, 074001 (2015). URL <https://dx.doi.org/10.1088/0264-9381/32/7/074001>.

209 4. Acernese, F. *et al.* Advanced virgo: a second-generation interferometric gravitational wave
210 detector. *Classical and Quantum Gravity* **32**, 024001 (2014). URL <https://dx.doi.org/10.1088/0264-9381/32/2/024001>.

212 5. Akutsu, T. *et al.* Overview of KAGRA: Detector design and construction history.
213 *Progress of Theoretical and Experimental Physics* **2021**, 05A101 (2020). URL <https://doi.org/10.1093/ptep/ptaa125>. <https://academic.oup.com/ptep/article-pdf/2021/5/05A101/37974994/ptaa125.pdf>.

216 6. Dwyer, S. *et al.* Gravitational wave detector with cosmological reach. *Phys. Rev. D* **91**, 082001
217 (2015). URL <https://link.aps.org/doi/10.1103/PhysRevD.91.082001>.

218 7. Punturo, M. *et al.* The einstein telescope: a third-generation gravitational wave observatory.
219 *Classical and Quantum Gravity* **27**, 194002 (2010). URL <https://dx.doi.org/10.1088/0264-9381/27/19/194002>.

221 8. Edwards, T. e. a. LISA: Study of the Laser Interferometer Space Antenna: Final Technical
222 Report (FTR), Dornier Satellitensysteme GmbH. Tech. Rep., DSS Report No. LI-RP-DS-009
223 (2000).

224 9. Tanvir, N. R. *et al.* A ‘kilonova’associated with the short-duration -ray burst grb 130603b.
225 *Nature* **500**, 547–549 (2013). URL <https://doi.org/10.1038/nature12505>.

226 10. Ascenzi, S. *et al.* A luminosity distribution for kilonovae based on short gamma-ray burst
227 afterglows. *Monthly Notices of the Royal Astronomical Society* **486**, 672–690 (2019). URL
228 <https://doi.org/10.1093/mnras/stz891>. <https://academic.oup.com/mnras/article-pdf/486/1/672/28320190/stz891.pdf>.

230 11. Jin, Z.-P. *et al.* A kilonova associated with grb 070809. *Nature Astronomy* **4**, 77–82 (2020).
231 URL <https://doi.org/10.1038/s41550-019-0892-y>.

232 12. Rastinejad, J. C. *et al.* A kilonova following a long-duration gamma-ray burst at
233 350 mpc. *Nature* **612**, 223–227 (2022). URL <https://doi.org/10.1038/s41586-022-05390-w>.

235 13. Albert, A. *et al.* Search for neutrino counterparts to the gravitational wave sources from
236 ligo/virgo o3 run with the antares detector. *Journal of Cosmology and Astroparticle Physics*
237 **2023**, 004 (2023). URL <https://dx.doi.org/10.1088/1475-7516/2023/04/004>.

239 14. Abbasi, R. *et al.* Icecube search for neutrinos coincident with gravitational wave events from
240 ligo/virgo run o3. *The Astrophysical Journal* **944**, 80 (2023). URL <https://dx.doi.org/10.3847/1538-4357/aca5fc>.

242 15. Harris, P. *et al.* Physics community needs, tools, and resources for machine learning (2022).
243 2203.16255.

244 16. Baltus, G. *et al.* Convolutional neural networks for the detection of the early inspiral of a
245 gravitational-wave signal. *Phys. Rev. D* **103**, 102003 (2021). URL <https://link.aps.org/doi/10.1103/PhysRevD.103.102003>.

247 17. Verma, C., Reza, A., Gaur, G., Krishnaswamy, D. & Caudill, S. Can convolution neural
248 networks be used for detection of gravitational waves from precessing black hole systems?
249 *arXiv preprint arXiv:2206.12673* (2022).

250 18. Krastev, P. G. Real-time detection of gravitational waves from binary neutron stars using
251 artificial neural networks. *Physics Letters B* **803**, 135330 (2020). URL <https://www.sciencedirect.com/science/article/pii/S0370269320301349>.

253 19. George, D. & Huerta, E. A. Deep neural networks to enable real-time multimessenger
254 astrophysics. *Phys. Rev. D* **97**, 044039 (2018). URL <https://link.aps.org/doi/10.1103/PhysRevD.97.044039>.

256 20. Nousi, P. *et al.* Deep residual networks for gravitational wave detection. *Phys. Rev. D* **108**,
257 024022 (2023). URL <https://link.aps.org/doi/10.1103/PhysRevD.108.024022>.

259 21. Online pipelines - igwn — public alerts user guide 2023 (2023). URL <https://emfollow.docs.ligo.org/userguide/analysis/searches.html>.

260

261 22. Skliris, V., Norman, M. R. K. & Sutton, P. J. Real-time detection of unmodelled

262 gravitational-wave transients using convolutional neural networks (2022). 2009.14611.

263

264 23. Paleyes, A., Urma, R.-G. & Lawrence, N. D. Challenges in deploying machine learning: A

265 survey of case studies. *ACM Comput. Surv.* **55** (2022). URL <https://doi.org/10.1145/3533378>.

266

267 24. Abbott, B. P. *et al.* Gwtc-1: A gravitational-wave transient catalog of compact binary mergers

268 observed by ligo and virgo during the first and second observing runs. *Phys. Rev. X* **9**, 031040

269 (2019). URL <https://link.aps.org/doi/10.1103/PhysRevX.9.031040>.

270

271 25. The LIGO Scientific Collaboration and the Virgo Collaboration *et al.* Gwtc-2.1: Deep

272 extended catalog of compact binary coalescences observed by ligo and virgo during the first

273 half of the third observing run (2022). 2108.01045.

274

275 26. Gebhard, T. D., Kilbertus, N., Harry, I. & Schölkopf, B. Convolutional neural networks:

276 A magic bullet for gravitational-wave detection? *Phys. Rev. D* **100**, 063015 (2019). URL

277 <https://link.aps.org/doi/10.1103/PhysRevD.100.063015>.

278

279 27. He, K., Zhang, X., Ren, S. & Sun, J. Deep residual learning for image recognition. In *2016*

280 *IEEE Conference on Computer Vision and Pattern Recognition (CVPR)*, 770–778 (2016).

281

282 28. Ioffe, S. & Szegedy, C. Batch normalization: Accelerating deep network training by reducing

283 internal covariate shift (2015). 1502.03167.

284

285 29. Wu, Y. & He, K. Group normalization. In *Proceedings of the European Conference on*

Computer Vision (ECCV) (2018).

30. Kingma, D. P. & Ba, J. Adam: A Method for Stochastic Optimization. *arXiv e-prints* arXiv:1412.6980 (2014). 1412.6980.

31. Smith, L. N. & Topin, N. Super-convergence: Very fast training of residual networks using

large learning rates. *CoRR* **abs/1708.07120** (2017). URL <http://arxiv.org/abs/1708.07120>. 1708.07120.

286 32. Gunny, A. *et al.* Hardware-accelerated inference for real-time gravitational-wave
287 astronomy. *Nature Astronomy* **6**, 529–536 (2022). URL <https://doi.org/10.1038/s41550-022-01651-w>.

289 33. Gunny, A. *et al.* A software ecosystem for deploying deep learning in gravitational
290 wave physics. In *Proceedings of the 12th Workshop on AI and Scientific Computing at*
291 *Scale Using Flexible Computing Infrastructures*, FlexScience ’22, 9–17 (Association for
292 Computing Machinery, New York, NY, USA, 2022). URL <https://doi.org/10.1145/3526058.3535454>.

294 **Acknowledgements** W.B and M.W.C acknowledge support from the National Science Foundation (NSF)
295 with grant numbers PHY-2010970 and PHY-2117997. E.M, E.K, A.G and D.C acknowledge support from
296 the NSF under award PHY-1764464 and PHY-2309200 to the LIGO Laboratory and PHY-2117997 to the
297 A3D3 Institute. E.M, E.K, A.G and D.C also acknowledge NSF awards PHY-1931469 and PHY-1934700
298 The authors express sincere gratitude to Reed Essick for clarifying numerous nuances of the sensitive volume
299 calculation. The authors are also very grateful to Thomas Dent for identifying a public dataset which could
300 be used to calculate the performance of traditional search pipelines. Additionally, the authors thank Vassilis
301 Skliris and Becca Ewing for their useful comments and discussion on earlier drafts of this work.
302 This research was undertaken with the support of the LIGO computational clusters. This material is based
303 upon work supported by the NSF’s LIGO Laboratory which is a major facility fully funded by the National
304 Science Foundation. This research has made use of data obtained from the Gravitational Wave Open Science
305 Center (www.gw-openscience.org), a service of LIGO Laboratory, the LIGO Scientific Collaboration and
306 the Virgo Collaboration.

307 **Correspondence** Correspondence and requests for materials should be addressed to Ethan Marx (emarx@mit.edu)
308 and Will Benoit (benoit090@umn.edu).

309 **Methods**

310 **1 Data**

311 **Strain.** We train and validate our neural-network using open data from the Gravitational Wave
312 Open Science Center (GWOSC)⁴⁷ between times 2019-04-29T13:29:25 and 2019-05-09T13:29:25,
313 corresponding to a ten calendar day period at the beginning of the O3 observing run. The strain
314 data is resampled to 2048 Hz for better computational efficiency. For each interferometer, we
315 query the openly available science mode flag to remove segments with poor data quality. We then
316 select segments for which the science mode flag is active for both the Hanford and Livingston
317 LIGO interferometers. This amounts to approximately 4.7 days of coincident livetime. We reserve
318 the segments that total a minimum of 15,000 seconds at the end of this period for validating the
319 neural-network throughout the training process.

320 For evaluating the performance reported in Fig. 2, we select data satisfying the above criteria
321 between times 2019-05-09T13:29:25 and 2019-06-08T13:29:25, corresponding to a 30 day period
322 immediately after the training period. This amounts to approximately 18 days of coincident
323 livetime. During evaluation, timeslides of this data are created such that the total desired background
324 time is achieved. We emphasize that no data used for evaluating the performance of the neural-network
325 was used during training or validation. In addition, we train the neural-network only with data from
326 before the testing period. This mimics the data availability scenario for real-time application.

327 **Waveforms.** We use `bilby`⁴⁸ to simulate 100,000 eight second long BBH waveforms at
328 2048 Hz with the IMRPhenomPv2 approximant⁴⁹. Out of these, 75,000 waveforms are used to
329 train the neural-network, and the remaining 25,000 are reserved for validation. To simulate a
330 waveform, a probability distribution is specified on each of the parameters that define a compact
331 binary merger, and random samples are drawn from each. The distribution set used in this work is
332 based on one used for GWTC-3⁵⁰ during O3 to assess the sensitivity of CBC search pipelines, and
333 is described in Table 2. The sampled parameters are used to compute the time-domain strain for
334 each polarization, h_+ and h_\times . The sampled component mass values are defined in the source frame,
335 so conversion to detector frame quantities is performed before generation. The interferometer
336 responses of the intrinsic polarizations are calculated during the training process to allow for
337 real-time data augmentations, as described below in Sec. 2.

338 The same distributions are used to simulate signals for the testing dataset. Enough waveforms

339 are generated to fill the background timeslides with the waveform coalescence points spaced 24 s
340 apart. As the signals are only 8 s long, they do not overlap. During the signal generation process,
341 we perform rejection sampling and keep only signals that have an SNR greater than 4. This ensures
342 that computation is not wasted on signals we do not expect to detect⁴⁴. Rejection sampling reduces
343 the uncertainty of a sensitive volume estimate for a fixed amount of analyzed injections (see Sec. 3).
344 In total, we generate $\sim 45,000,000$ waveforms. Of these, $\sim 3\%$ percent are used for testing and
345 $\sim 97\%$ are rejected.

346 2 Training

347 We apply several data augmentation techniques during the training process with the goal of providing
348 robust, high entropy data that encodes physics-based knowledge for discriminating signals from
349 noise. Below, we will describe how a training batch is composed, as well as the hyper-parameters
350 that control the composition of the batches.

351 **Noise sampling.** Sampled at 2048 Hz, the entire training dataset is unable to fit onto a
352 single 16 GB V100 GPU at once. Thus, efficient out-of-memory data-loading is required to fully
353 utilize the extent of our strain dataset. To do this, we sample strain windows directly from disk
354 during the training procedure. The length of each noise window sampled from disk is 10.5 s.
355 The first 8 s is used to estimate the power spectral density (PSD) used for whitening. We use
356 Welch's method to estimate the PSD. The remaining 2.5 s of the window is whitened in the
357 frequency-domain, and transformed back to time-domain. Due to whitening filter settle-in, 0.5 s
358 of data is corrupted on both ends of the window and removed. Thus, only 1.5 s of data is actually
359 analyzed by the neural-network. The PSD estimation, filter construction, and whitening are all
360 done with PyTorch⁵¹ modules to enable GPU-accelerated computation²⁰. We use a training
361 batch size of 384, which was chosen such that we fully utilize the GPU memory available. Our
362 out-of-memory data-loading is sufficiently fast to support these batch sizes without bottle-necking
363 the pre-processing or neural-network modules.

364 Noise instances are sampled independently in time from each interferometer. Thus, a noise
365 instance from one interferometer can be paired with many different instances from the other
366 interferometer. This combinatorially increases the amount of unique two-detector noise instances
367 available for optimizing the network. Next, each noise instance has probability p_{invert} to be inverted
368 ($h(t) \rightarrow -h(t)$) and, independently, probability p_{reverse} to be reversed ($h(t) \rightarrow h(-t)$)⁵³. Again, the

Parameter	Description	Prior	Limits	Units
m_1	Mass of primary	$m_1^{-2.35}$	(5, 100)	M_\odot
m_2	Mass of secondary	m_2	(5, m_1)	M_\odot
z	Redshift	Comoving	(0, 2)	-
ψ	Polarization angle	Uniform	(0, π)	rad.
$a_{1,2}$	Dimensionless spin magnitude	Uniform	(0, 0.998)	-
$\theta_{1,2}$	Spin tilt	Sine	(0, π)	rad.
ϕ_{12}	Relative spin azimuthal angle	Uniform	(0, 2π)	rad.
ϕ_{JL}	Spin phase angle	Uniform	(0, 2π)	rad.
ϕ	Orbital phase	Uniform	(0, 2π)	rad.
RA	Right ascension	(0, 2π)	rad.	
Dec	Declination	Cosine	($-\pi/2$, $\pi/2$)	rad.
θ_{JN}	Inclination angle	Sine	(0, π)	rad.

Table 2: Priors on parameters used to generate waveforms for both the training and testing sets. The prior is derived from that used in GWTC-3 to assess search pipelines. The component mass distributions are defined in the source frame. 'Comoving' refers to uniform in comoving volume.

Parameter	Description	Prior	Limits	Best Value
lr_{max}	Maximum learning rate	Log Uniform	$(10^{-4.5}, 10^{-2})$	5.8×10^{-4}
N_{ramp}	Number of epochs over which learning rate increases	Uniform	(2, 50)	23
p_{signal}	Probability of batch element containing a signal	Uniform	(0.2, 0.6)	0.277
p_{swap}	Probability of swap augmentation	Uniform	(0, 0.15)	0.014
p_{mute}	Probability of mute augmentation	Uniform	(0, 0.3)	0.055
SNR steps	Number of batches over which SNR scheduler decays	Uniform	(1, 2500)	989

Table 3: Priors and descriptions of hyperparameters searched over. The best value corresponds to the neural-network from the hyperparameter search that produced the highest validation score across all epochs. A neural-network trained with these hyperparameters was used to evaluate results reported in Fig. 2. Details on hyperparameters can be found in Sec. 2

369 inversion and reversal augmentations increase the amount of unique noise instances in our training
370 data. For transient noise, these augmentations increase the variety of morphologies provided during
371 training, allowing for better generalization to unseen testing data. We fix p_{invert} and p_{reverse} to 0.5.

372 **Signal Injection.** Once a batch of noise instances is generated, simulated BBH signals
373 are added into each 2.5 s unwhitened window with probability $p_{\text{signal}} = 0.277$ and labeled as
374 signals; this signal probability is one of six hyperparameters that we search over (see Table 3
375 and the discussion of hyperparameters below). The procedure for injecting signals is as follows:
376 first, intrinsic polarization time-series are randomly sampled from the training waveform bank.
377 Next, random extrinsic parameters (right ascension, declination, polarization angle, and SNR) are
378 sampled. The first three of these are sampled from the priors described in Table 2; We will discuss
379 the method of SNR sampling in the following paragraph. Intrinsic polarization time-series are
380 then projected onto the interferometers and re-scaled to the sampled SNR. Randomly sampling
381 extrinsic parameters at training time allows each intrinsic time-series to be injected from a variety
382 of sky localizations and distances throughout the training procedure. We found that standard CPU
383 implementations of projecting intrinsic polarizations onto interferometers created bottlenecks that
384 severely limited utilization of GPU resources. We eliminated this bottleneck by developing a
385 PyTorch⁵¹ implementation so that projection can be accelerated using GPUs by a factor of ~ 200 .
386 Finally, the interferometer responses are added into the noise instances. The coalescence time of
387 the merger is randomly placed so that it falls at least 0.25 s from either edge of the 1.5 s whitened
388 noise instance. We enforce this padding because we found that having the coalescence point too
389 close to the left edge of the window makes it more difficult for the neural-network to learn, since
390 much of the signal SNR would lie outside the window. The random placement of the coalescence
391 time encodes time translational invariance so that the neural-network can identify signals with the
392 coalescence time at different locations throughout the window.

393 **Curriculum Learning.** Curriculum learning is a technique for training machine learning
394 models in which initially, easy to learn samples are provided as training data, and progressively
395 harder samples are introduced over time. One way to apply this in the context of GW detection is
396 to initially provide high SNR signals and gradually introduce lower SNR signals²⁰. This allows the
397 neural-network to quickly arrive at a minima of its parameter space before trying to optimize for
398 the more realistic task. We begin with an SNR distribution that follows a power law, $p(\text{SNR}) \sim$
399 $(\text{SNR})^{-3}$, with a minimum of $\text{SNR}_{\text{min}} = 12$ and a maximum of $\text{SNR}_{\text{max}} = 100$. The form of this
400 distribution was chosen to roughly match the SNR distribution of our astrophysically motivated

401 prior. Each time a new training batch is constructed, the minimum SNR bound of the distribution
402 is decreased until we reach the ultimate lower bound of 4. This decrease happens uniformly over
403 989 batches, a value that was reached through a hyperparameter search.

404 **Glitch Mitigation.** Non-Gaussian noise transients, known as “glitches,” can often mimic
405 BBH signals and lead to high-significance false alarms. We implement two types of augmentations
406 we call waveform *muting* and *swapping* to mitigate the impact of transient glitches. These augmentations
407 respectively encode the concepts of coincidence and coherence that true astrophysical signals are
408 expected to exhibit. The values of the parameters controlling these augmentations were determined
409 by hyperparameter search; see below for more details.

410 *Muting:* For a fraction $p_{\text{mute}} = 0.055$ of the training batch, we inject a BBH signal into only
411 one of the interferometers and label these samples as noise. This teaches the neural-network that it
412 is not enough for a BBH-like signal to be present in just one interferometer: coincidence between
413 interferometers is a requirement for true astrophysical signals.

414 *Swapping:* For an independent fraction of the training batch, $p_{\text{swap}} = 0.014$, we swap one
415 of the interferometer responses with an interferometer response from different signal, and label
416 these samples as noise. Thus, these windows will contain BBH waveforms with different intrinsic
417 parameters in each interferometer. This motivates the neural-network to learn the concept of
418 coherence: the time-frequency evolution of the signal must be identical in both interferometers.

419 **Algorithm Longevity.** Noise in gravitational wave interferometers is non-stationary. Therefore,
420 the timescale over which a single trained neural-network will maintain its originally measured
421 performance needs to be evaluated. Determining this timescale helps inform the cadence at which
422 retraining is needed, if at all. To test the longevity of our algorithm, we construct several testing
423 datasets at various intervals across O3. For each interval, we analyze the testing dataset with a
424 neural-network trained using the first 10 days of O3 data. This is the same neural-network used to
425 produce the results in Fig. 2. To separate the sensitivity of the neural-network from the sensitivity
426 of the detectors, we do not measure sensitive volume, but instead look at the fraction of events
427 with $\text{SNR} > 8$ that are detected at different FARs. This metric takes into account the variation
428 in noise level across different time periods, though it does not account for all aspects of detector
429 performance, such as the rate or morphology of glitches. At a FAR of 1 event per 2 months, a
430 threshold comparable to the 1 event per 5 months used for releasing significant public alerts by

431 the IGWN^b, we see in Fig 4 that the fractional detection rate of the original neural-network does
 432 not decay with time. We note that the most significant background event across all weeks is found
 433 during week 2, corresponding to the sharp drop in detection fraction at a FAR of 1 per 2 months.
 434 Though there is some fluctuation from week to week, a single neural-network trained on a week's
 435 worth of data at the beginning of the observing run maintains sensitivity over the duration of the
 436 run.

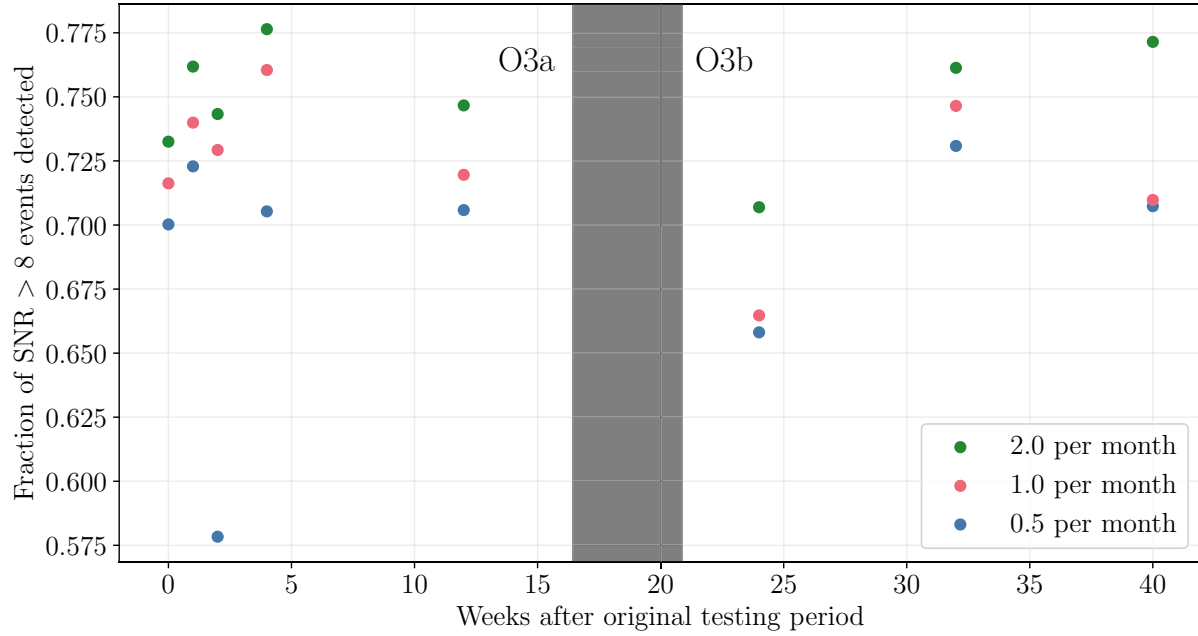


Figure 4: The fraction of $\text{SNR} > 8$ events detected at different false alarm rates during various weeks across a period of time during O3, beginning May 9th, 2019 and ending March 21st, 2020. Errors on detection fraction estimates are smaller than the plotted points.

437 **Validation.** We construct our validation procedure with the goal of establishing a strong
 438 correlation between validation and test metrics. This allows us to confidently pick the best performing
 439 neural-network during a hyperparameter search, as well as during individual training runs. To
 440 accomplish this, our validation procedure is designed to mimic the testing procedure as closely as
 441 possible. We reserve 15,000 seconds of strain data from immediately after the training period and
 442 25,000 waveforms exclusively for neural-network validation during training. This data is not used
 443 at all for training the neural-network. This temporal choice of training and validation split mimics

^b<https://emfollow.docs.ligo.org/userguide/analysis/>

444 the real-time production setting, where a deployed neural-network is only trained on past data.

445 To construct our validation set, we first create timeslides of the background data until at least
446 16 hours of livetime is accumulated. Similarly to training, this data is batched into 10.5 s windows,
447 with the first 8 s used for whitening the final 2.5 s of each window. As with the training data,
448 0.5 s of data is cropped from each edge of the window after whitening. Next, we create a dataset
449 of injections by adding waveforms from the validation waveform dataset into the background
450 windows. We set a minimum detector-network SNR threshold of 4 for validation signals. Signals
451 that are quieter are re-scaled to the SNR 4 threshold. The SNR is computed with respect to the
452 PSD calculated from the first 8 s of the window. This rescaling procedure mimics the SNR-based
453 rejection sampling performed for the testing dataset. We create 5 unique injection sets that have
454 the coalescence point of each waveform at 0.25, 0.5, 0.75, 1.0, and 1.25 s within each whitened
455 window. This ensures the validation metric covers a wider variety of scenarios.

456 The neural-network outputs a prediction for each window in the background and injection
457 datasets. We use these predictions to calculate the area under the ROC curve (AUROC) up to a false
458 positive rate (FPR) of 10^{-3} , which is the final validation metric. We make this cut on the AUROC
459 so that we are optimizing performance in the regime of low FARs. After the neural-network
460 training has converged, the weights corresponding to the epoch with the highest validation score
461 are used for testing.

462 **Hyperparameter Search.** The hyperparameters of our algorithm are optimized via a
463 random search⁵⁴. It is infeasible to search over all possible hyperparameters, so we selected those
464 that we a-priori expect to have the greatest impact on the neural-network optimization process.
465 These were the neural-network’s maximum learning rate (lr_{\max}), the number of epochs over which
466 the learning rate “ramps up” (N_{ramp}) to lr_{\max} , p_{signal} , p_{mute} , p_{swap} , and the number of steps over
467 which SNR curriculum learning was performed. The priors on each of these parameters can
468 be found in Table 3. 30 combinations of these parameters were randomly sampled and used to
469 train a neural-network. Of these, the neural-network that reported the highest validation score was
470 selected as the neural-network used for testing. The hyperparameters used to train this neural-network
471 are reported in Table 3.

472 **3 Sensitive Volume**

473 A key metric in understanding a search algorithm's performance is the *sensitive volume*, which is
 474 a measure of the region of space in which a pipeline is expected to detect merging binaries. The
 475 sensitive volume as a function of the FAR is defined by

$$V(\mathcal{F}) = \int d\mathbf{x} d\theta \epsilon(\mathcal{F}; \mathbf{x}, \theta) \phi(\mathbf{x}, \theta) \quad (1)$$

476 where ϕ is the distribution of events over spatial coordinates \mathbf{x} and binary system parameters
 477 θ , and ϵ is the detection efficiency of the pipeline at a false alarm rate \mathcal{F} ⁵⁵. Generally, this
 478 quantity is estimated using Monte-Carlo integration by drawing waveforms from a population
 479 model, injecting them into a background, and counting how many produce triggers below a given
 480 false alarm rate threshold. If the samples are drawn from within the redshifted volume⁵⁶ V_0 , with

$$V_0 = \int_{z_{\min}}^{z_{\max}} dz \frac{dV_c}{dz} \frac{1}{1+z} \quad (2)$$

481 where dV_c/dz is the differential comoving volume, then the sensitive volume is approximately

$$V(\mathcal{F}) \approx V_0 \frac{N(\mathcal{F})}{N_{\text{draw}}} \quad (3)$$

482 where $N(\mathcal{F})$ is the number of signals detected at a FAR less than \mathcal{F} and N_{draw} is the number of
 483 injected events.

484 It is often desired to quantify the sensitivity of an algorithm to different populations. For
 485 example, an algorithm's sensitivity may vary with different source masses. Through the technique
 486 of importance sampling, it is possible to use one injection set from a broad population to calculate
 487 the sensitive volume for several populations. Each injection is weighted by the ratio of the probability
 488 of having been drawn from the injected distribution to that of the population distribution of interest⁵⁷:

489

$$V_{\text{pop}}(\mathcal{F}) \approx \frac{V_0}{N_{\text{inj}}} \sum_{i=1}^{N(\mathcal{F})} \frac{p_{\text{pop}}(\theta_i)}{p_{\text{inj}}(\theta_i)} \quad (4)$$

490 The Monte-Carlo uncertainty on this estimation is⁵⁸

$$(\delta V_{\text{pop}})^2 = \frac{V_0^2}{N_{\text{inj}}^2} \sum_{i=1}^{N(\mathcal{F})} \left(\frac{p_{\text{pop}}(\theta_i)}{p_{\text{inj}}(\theta_i)} \right)^2 - \frac{V_{\text{pop}}^2}{N_{\text{inj}}} \quad (5)$$

491 The SNR-based rejection performed during the generation of test set waveforms is done to improve
492 this uncertainty. Waveforms that are sampled but have an SNR less than 4 are not injected;
493 however, they still count towards N_{draw} . The cut is placed such that any waveforms below the
494 SNR cutoff are not expected to be recovered at any reasonable FAR, and so would not contribute
495 to the sensitive volume: whether injected or not, their weight would be zero. This procedure
496 allows us to effectively draw many times more samples than are actually injected, greatly reducing
497 the uncertainty on the sensitive volume. For this analysis, we re-weight to the same population
498 distributions used in the sensitive volume analysis conducted in GWTC-3², log-normal distributions
499 about central masses of interest with widths of 0.1. In addition, we enforce time difference of
500 no more than 0.25 s between the recovered and injected coalescence times. This time difference
501 corresponds to the resolution available at an inference sampling rate of 4 Hz. This time resolution
502 can be reduced by increasing the inference sampling rate.

503 4 Inference

504 Our inference pipeline is an ensemble of three models: a snapshotter³³, a whitener, and the
505 neural-network itself. Clients send streaming updates of strain data to a snapshotter. The snapshotter
506 sends the latest state to the whitening module. Finally, batches of whitened data are constructed
507 and analyzed by `Aframe`, producing predictions. The length of the state maintained by the
508 snapshotter is determined by the length of the timeseries used to estimate the PSD, the batch size,
509 and the inference sampling rate. For our analysis, the whitening module uses the first 64 seconds
510 of the snapshotter state to estimate the PSD and build a whitening filter. The remaining data is
511 whitened, and half a second is cropped from both edges to remove the effects of filter settle-in.
512 The whitened data is then unfolded into a batch of overlapping windows. We use a batch size of
513 128 windows, and, as an inference sampling rate of 4 Hz was used, each 1.5 s window overlaps its
514 neighbors by 1.25 s. This batch of windows is passed to the neural-network for prediction. Lastly,
515 neural-network predictions are aggregated client-side and post-processed via the integration and
516 clustering described above.

517 For an online analysis, the pre- and post-processing steps incur a total latency of approximately
518 3.1 s, see Table 4 for a summary. The most significant source of latency in the online analysis
519 comes from waiting for data to exist such that we can crop the edges after resampling and whitening.
520 All other computational steps (data reading/writing, data transfer to/from GPU, whitening, event
521 identification, etc.) take less than 0.4 seconds combined, while the inference step itself takes less

522 than 10 milliseconds. An additional source of latency is the means by which live data is made
523 available during an observation run. New data is written out in 1 s segments. Thus, depending on
524 where the coalescence point of an event falls within one of these segments, it may be necessary to
525 wait for a full additional second for a file to be written before event identification can occur. This
526 factor is not included in Table 4, nor is the time it takes for data to become available, or the time
527 taken to upload a candidate event to GraceDB, as none of these processes is within our control.

528 A critical parameter is the inference sampling rate. The inference sampling rate controls
529 the stride between consecutive windows seen by the neural-network. Too small of an inference
530 sampling rate, and astrophysical events may be skipped over. Too large, and computing resources
531 are wasted on redundant inferences. We examined the impact of the inference sampling rate on
532 our sensitivity by repeating trials of our inference procedure at inference sampling rates of 1, 2, 4,
533 8, 16 and 64 Hz. For this analysis, we accumulated two months worth of timeslide data for each
534 trial. Fig. 5 shows a subset of the results of this analysis. Algorithms mostly perform within their
535 statistical error. However, at low FARs the 1 Hz analysis has a small performance dip in the 35-35
536 mass bin. Because analyses performed at 4 Hz require 16 times fewer inference requests than
537 64 Hz without sacrificing performance, we use an inference sampling rate of 4 Hz for the analyses
538 in this paper.

539 **5 Data and Software Availability**

540 All code used to produce results in this work is publicly available. The `Aframe` project repository
541 can be found at <https://github.com/ML4GW/aframe>.

542 In addition, two open source libraries, `ml4gw`^c and `hermes`^d were developed to support this
543 work. The `ml4gw` library contains PyTorch utilities for efficient on-GPU data-loading, whitening,
544 PSD estimation and other data processing techniques common to GW analysis. The `hermes`
545 library contains utilities for deploying models in the IaaS paradigm via Triton Inference Servers.

^c<https://github.com/ML4GW/ml4gw>

^d<https://github.com/ML4GW/hermes>

Latency Source	Latency (s)
Coalescence point exiting training kernel padding	0.25
Cropping corruption from whitening filter	0.50
Cropping corruption from resampling to 2048 Hz	1.0
Integrating neural-network output	1.0
Reading data and transferring to GPU	$1.03_{-0.05}^{+0.06} \times 10^{-2}$
Estimating PSD and whitening	$8.77_{-0.31}^{+1.35} \times 10^{-4}$
Performing inference on whitened data	$9.63_{-0.32}^{+0.38} \times 10^{-3}$
Integrating and aggregating neural-network output	$3.42_{-0.01}^{+0.02} \times 10^{-1}$
Identifying candidate events in integrated output	$1.40_{-0.43}^{+0.62} \times 10^{-4}$
Total	$3.114_{-0.001}^{+0.006}$

Table 4: Sources of latency for an `Aframe` online analysis. For the items listed in the upper section this table, the latency does not come from performing the computation, but rather from needing to wait for the data to exist before the action can occur. Items in the lower section are computational steps, and we report the median timing of 9191 trials. The upper and lower error bars represent the 95th and 5th percentile, respectively. All measurements were taken on a dedicated NVIDIA A30 GPU.

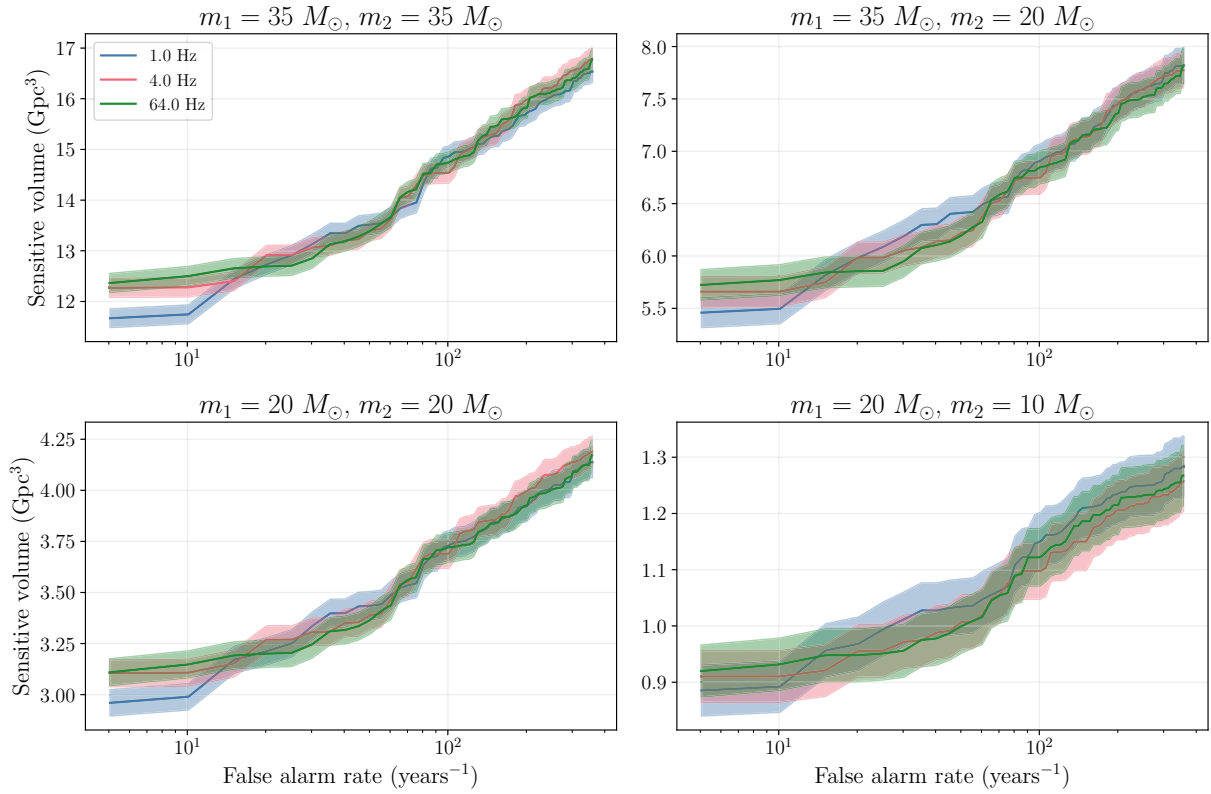


Figure 5: Sensitivity comparisons for the same neural-network run over the same data at different inference rates. For the purposes of clarity, only a subset of the tested rates are shown here. Except for the 1 Hz inference, all results are within error of each other for all mass combinations and FARs, including for rates not shown in this plot.

546 **References**

547 34. NVIDIA Corporation. Triton Inference Server: An Optimized Cloud and Edge Inferencing
548 Solution. (2023). URL <https://github.com/triton-inference-server/>
549 server.

550 35. Huerta, E. A. *et al.* Accelerated, scalable and reproducible ai-driven gravitational wave
551 detection. *Nature Astronomy* **5**, 1062–1068 (2021). URL <https://doi.org/10.1038/s41550-021-01405-0>.

553 36. Abbott, R. *et al.* Gwtc-3: Compact binary coalescences observed by ligo and virgo during the
554 second part of the third observing run. *Physical Review X* **13** (2023). URL <http://dx.doi.org/10.1103/PhysRevX.13.041039>.

556 37. Aubin, F. *et al.* The MBTA pipeline for detecting compact binary coalescences in the third
557 LIGO–virgo observing run. *Classical and Quantum Gravity* **38**, 095004 (2021). URL
558 <https://doi.org/10.1088%2F1361-6382%2Fabe913>.

559 38. Canton, T. D. *et al.* Real-time search for compact binary mergers in advanced ligo and virgo’s
560 third observing run using pycbc live. *The Astrophysical Journal* **923**, 254 (2021). URL
561 <https://dx.doi.org/10.3847/1538-4357/ac2f9a>.

562 39. Ewing, B. *et al.* Performance of the low-latency gstdlal inspiral search towards ligo, virgo, and
563 kagra’s fourth observing run (2023). [2305.05625](https://arxiv.org/abs/2305.05625).

564 40. Tsukada, L. *et al.* Improved ranking statistics of the GstLAL inspiral search for compact
565 binary coalescences. *Physical Review D* **108** (2023). URL <https://doi.org/10.1103%2Fphysrevd.108.043004>.

567 41. Drago, M. *et al.* coherent waveburst, a pipeline for unmodeled gravitational-wave data
568 analysis. *SoftwareX* **14**, 100678 (2021). URL <https://www.sciencedirect.com/science/article/pii/S2352711021000236>.

570 42. Schäfer, M. B. *et al.* First machine learning gravitational-wave search mock data challenge.
571 *Phys. Rev. D* **107**, 023021 (2023). URL <https://link.aps.org/doi/10.1103/PhysRevD.107.023021>.

573 43. Chaturvedi, P., Khan, A., Tian, M., Huerta, E. A. & Zheng, H. Inference-optimized ai and
574 high performance computing for gravitational wave detection at scale. *Frontiers in Artificial*
575 *Intelligence* **5** (2022). URL <http://dx.doi.org/10.3389/frai.2022.828672>.

576 44. LIGO Scientific Collaboration, Virgo Collaboration & KAGRA Collaboration. GWTC-3:
577 Compact Binary Coalescences Observed by LIGO and Virgo During the Second Part of the
578 Third Observing Run — O3 search sensitivity estimates (2023). URL <https://doi.org/10.5281/zenodo.7890437>.

580 45. The LIGO Scientific Collaboration and the Virgo Collaboration *et al.* Gwtc-2.1: Deep
581 extended catalog of compact binary coalescences observed by ligo and virgo during the first
582 half of the third observing run (2022). [2108.01045](https://doi.org/10.5281/zenodo.7890437).

583 46. Chaudhary, S. S. *et al.* Low-latency gravitational wave alert products and their performance
584 in anticipation of the fourth ligo-virgo-kagra observing run (2023). [2308.04545](https://doi.org/10.5281/zenodo.7890437).

585 47. The LIGO Scientific Collaboration and the Virgo Collaboration and the KAGRA
586 Collaboration *et al.* Open data from the third observing run of ligo, virgo, kagra, and geo.
587 *The Astrophysical Journal Supplement Series* **267**, 29 (2023). URL <https://doi.org/10.3847/1538-4365/acdc9f>.

589 48. Ashton, G. *et al.* Bilby: A user-friendly bayesian inference library for gravitational-wave
590 astronomy. *The Astrophysical Journal Supplement Series* **241**, 27 (2019). URL <https://doi.org/10.3847/1538-4365/ab06fc>.

592 49. Hannam, M. *et al.* Simple model of complete precessing black-hole-binary gravitational
593 waveforms. *Phys. Rev. Lett.* **113**, 151101 (2014). URL <https://doi.org/10.1103/PhysRevLett.113.151101>.

595 50. Abbott, R. *et al.* Population of merging compact binaries inferred using gravitational waves
596 through gwtc-3. *Phys. Rev. X* **13**, 011048 (2023). URL <https://doi.org/10.1103/PhysRevX.13.011048>.

598 51. Paszke, A. *et al.* *PyTorch: An Imperative Style, High-Performance Deep Learning Library*
599 (Curran Associates Inc., Red Hook, NY, USA, 2019).

600 52. Nousi, P. *et al.* Deep residual networks for gravitational wave detection. *Phys. Rev. D* **108**,
601 024022 (2023). URL [https://link.aps.org/doi/10.1103/PhysRevD.108.](https://link.aps.org/doi/10.1103/PhysRevD.108.024022)
602

603 53. Bini, S., Vedovato, G., Drago, M., Salemi, F. & Prodi, G. A. An autoencoder neural network
604 integrated into gravitational-wave burst searches to improve the rejection of noise transients.
605 *Classical and Quantum Gravity* **40**, 135008 (2023). URL <https://doi.org/10.1088%2F1361-6382%2Facd981>.

607 54. Bergstra, J. & Bengio, Y. Random search for hyper-parameter optimization. *J. Mach. Learn.
608 Res.* **13**, 281–305 (2012).

609 55. Schäfer, M. B., Ohme, F. & Nitz, A. H. Detection of gravitational-wave signals from binary
610 neutron star mergers using machine learning. *Phys. Rev. D* **102**, 063015 (2020). URL <https://link.aps.org/doi/10.1103/PhysRevD.102.063015>.

612 56. Chen, H.-Y. *et al.* Distance measures in gravitational-wave astrophysics and cosmology.
613 *Classical and Quantum Gravity* **38**, 055010 (2021). URL <https://dx.doi.org/10.1088/1361-6382/abd594>.

615 57. Tiwari, V. Estimation of the sensitive volume for gravitational-wave source populations using
616 weighted monte carlo integration. *Classical and Quantum Gravity* **35**, 145009 (2018). URL
617 <https://dx.doi.org/10.1088/1361-6382/aac89d>.

618 58. Farr, W. M. Accuracy requirements for empirically measured selection functions. *Research
619 Notes of the AAS* **3**, 66 (2019). URL <https://dx.doi.org/10.3847/2515-5172/ab1d5f>.

621 59. Gunny, A. *et al.* A software ecosystem for deploying deep learning in gravitational
622 wave physics. In *Proceedings of the 12th Workshop on AI and Scientific Computing at
623 Scale Using Flexible Computing Infrastructures*, FlexScience '22, 9–17 (Association for
624 Computing Machinery, New York, NY, USA, 2022). URL <https://doi.org/10.1145/3526058.3535454>.